Materials & Design 232 (2023) 112143

Contents lists available at ScienceDirect

Materials & Design

journal homepage: www.elsevier.com/locate/matdes

Hardening effect of diffusible hydrogen on BCC Fe-based model alloys by *in situ* backside hydrogen charging

Jing Rao [a], Subin Lee [a,b], Gerhard Dehm [a,*], María Jazmin Duarte [a,*]

[a] Max-Planck-Institut für Eisenforschung, Max-Planck-Straße 1, 40237 Düsseldorf, Germany
[b] Now at: Institute for Applied Materials (IAM), Karlsruhe Institute of Technology, Hermann-von-Helmholtz-Platz 1, 76344, Eggenstein-Leopoldshafen, Germany

HIGHLIGHTS

- The effect of diffusive vs. deeply trapped hydrogen is deduced by time-dependent evolution of mechanical properties for ferritic alloys using novel in-situ nanoindentation during backside continuous hydrogen supply.
- A linear relationship between hardness increase and hydrogen ingress is observed in the initial stage, with a more pronounced hardening effect for higher content of the studied substitutional elements.
- An increase in dislocation density due to hydrogen is quantified by transmission electron microscopy.
- Our data support the interpretation that hydrogen facilitates dislocation nucleation in the initial stage following the defactant theory; and we link the hardness increase to the dislocation density and friction stresses arising from diffusible hydrogen.

GRAPHICAL ABSTRACT

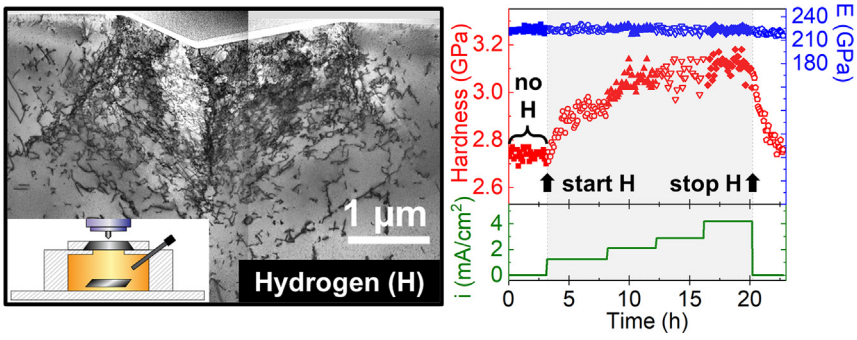

ARTICLE INFO

Article history:
Received 1 May 2023
Revised 13 June 2023
Accepted 4 July 2023
Available online 8 July 2023

Keywords:
bcc FeCr alloys
Hydrogen embrittlement
In situ nanoindentation
Hardness
Elastic modulus
Diffusible hydrogen

ABSTRACT

Hydrogen embrittlement is common in metallic materials and a critical issue in industries involving hydrogen-related processes. Here we investigate the mechanical response upon hydrogen loading of ferritic Fe-16Cr, Fe-21Cr and Fe-4Al alloys. We use a novel *in situ* setup for electrochemical backside hydrogen charging during nanoindentation. Single-phase ferritic Fe-Cr binary alloys with high hydrogen diffusivity and low solubility, are ideal for *in situ* studies during hydrogen charging, particularly the effect of diffusible and lightly trapped hydrogen is targeted. The hardness increases linearly with increasing hydrogen content until a quasi-equilibrium state between hydrogen absorption and desorption is reached while Young's modulus remains unaffected. Above this transient region, the slope of the absolute hardness experiences a drastic decrease. The hardness variation in Fe-21Cr is anisotropic as determined for (100), (110) and (111) oriented grains. Increasing the Cr content enhances the hardening effect in (100) orientation: a 16.7 % hardness increase is observed in Fe-21Cr, while Fe-16Cr, shows an increment of 10.8 %. A Fe-4Al alloy increases slightly in hardness by only 4.3 % at the applied current density of

* Corresponding authors.
E-mail addresses: dehm@mpie.de (G. Dehm), j.duarte@mpie.de (M.J. Duarte).

https://doi.org/10.1016/j.matdes.2023.112143

3 mA/cm^2. The hardening effect is caused by enhancing dislocation density, as revealed by studying the cross-section underneath the nanoindentation imprints.

1. Introduction

Hydrogen is a promising candidate as energy carrier for the near-future clean power industry, by reducing carbon dioxide emissions compared to fossil fuels. However, the proposed "hydrogen economy" still faces challenges due to material degradation phenomena, known as hydrogen embrittlement (HE), occurring during hydrogen production, transport and storage processes [1,2]. HE often leads to catastrophic brittle failure and unpredictable fracture of metals. Although HE has been widely explored, there is still a lack of fundamental understanding and controversial interpretations about its specific effects and interaction mechanisms in steels and other materials.

Ferritic bcc Fe alloys have high hydrogen diffusivity and low hydrogen solubility [1,3]. At ambient temperature and atmospheric pressure, the diffusivity of hydrogen through interstitial sites in pure and undeformed α-Fe is between 10^{-5} to 10^{-4} cm^2/s [4]. Particularly critical is to understand the role of this highly diffusive hydrogen as often it has a stronger influence on HE processes than deeply trapped hydrogen. In addition, Cr and Al are prominent alloying elements frequently employed in ferritic stainless steels, which find extensive application in industries exposed to challenging conditions such as severe radiation, humidity, and corrosive environments [2,5]. In such scenarios, the occurrence of hydrogen embrittlement becomes highly probable, consequently impairing the material properties. Investigating the influence of these elements is crucial in providing insights for the design of future alloys aimed at mitigating hydrogen embrittlement. Furthermore, based on simulations in ferritic steels, the binding energy of hydrogen to Cr is 26–27 kJ/mol and ~ 6 kJ/mol in the case of Al [4,6,7]. Consequently, Cr and Al are considered reversible hydrogen trapping sites in ferritic alloys. By incorporating higher concentrations of Cr and Al, more hydrogen can potentially be trapped within the material, amplifying the embrittlement effect, facilitating its detection and enabling more comprehensive investigations.

Ex situ hydrogen charging experiments, which focus on post characterization, have been widely used to investigate the mechanical properties and microstructural changes because of their relatively easy experimental procedure. For example, after electrochemically charging an austenitic steel, AISI 304L, with deuterium (D), the D distribution can be recorded during bending tests using time-of-flight secondary ion mass spectrometry (ToF-SIMS) [8]. Moreover, Park et al. [9] observed a hydrogen-induced hardening effect by nanoindentation in an austenitic stainless steel through *ex situ* electrochemical charging, connecting hardening to solid solution strengthening and hydrogen-enhanced planar slip. Since fcc materials can store a larger amount of hydrogen over longer periods of time than bcc alloys, they are more frequently applied in *ex situ* hydrogen charging tests [10,11]. However, outgassing and desorption of hydrogen during the tests are inevitable, leading to hydrogen concentration gradients.

Recently, novel *in situ* hydrogen charging methods have been introduced to investigate the diffusible hydrogen effects in materials with high hydrogen diffusion rates. They range from plasma charging inside the scanning electron microscope (SEM) chamber [12] to e-beam irradiation by environmental transmission electron microscopy (TEM) [13], where possible beam damage to the specimens is unpreventable. Electrochemical nanoindentation (ECNI), introduced by Barnoush and Vehoff in 2006 [14], has as well attracted attention to explore HE. Nanoindentation has a high lateral resolution of nanometer-scale, allowing the investigation of intrinsic mechanical properties such as dislocation nucleation stress, elasticity, and hardness, without the convoluting influence of grain boundaries and other microstructural features. Barnoush et al. [14,15] observed a pop-in load decrease in single-crystal Ni (1 1 1) during hydrogen charging, attributed to homogeneous dislocation nucleation in materials with low intrinsic dislocation density. Therefore, they explained the influence of hydrogen by a reduction of the interatomic bonds and stacking fault energy in Ni. After following studies on Fe-40 at.% Al, Fe-3 wt% Si, Al and Cu [16], Barnoush and Vehoff suggested that a reduction of the dislocation line energy by hydrogen ("defactant theory" [17]) caused the easier homogeneous dislocation nucleation. They concluded that neither the original form of hydrogen-enhanced localized plasticity nor the hydrogen-enhanced decohesion mechanisms solely are sufficient to explain HE [16]. They suggested that the reduction in the dislocation line energy and stacking fault energy as explained by the defactant theory combined with the reduction in lattice cohesion can successfully describe HE [16,17]. Further research on the hardness evolution upon hydrogen charging was conducted using ECNI in Fe-22Mn-0.6C steel [18], nickel alloy 725 [19], and high-entropy alloy [20]. The observed hardness enhancement was explained by increased lattice friction and solid solution strengthening. Hydrogen softening is typically explained by the hydrogen-enhanced localized plasticity and adsorption-induced dislocation-emission mechanisms, in which both, the dislocation mobility and nucleation rate, are enhanced and thus the yield strength or/and tensile strength are decreased. However, during the ECNI technique, chemical reactions occurring between the electrolyte and the probed sample might alter the microstructure, chemistry or surface topography of the specimen, introducing stress localization [21]. These drawbacks increased the interest in backside hydrogen-charging methods [12,22].

In this study, we have applied a novel *in situ* nanoindentation setup to systematically investigate the hydrogen effects on the deformation and mechanical properties of single-phase ferritic Fe-16Cr, Fe-21Cr and Fe-4Al alloys. The advantage of our approach with respect to ECNI or frontside charging is that the sample surface topography and chemistry remain unaltered throughout electrochemical hydrogen charging, which is conducted from the backside. This allows reliable post-characterization analyses, as well as getting precise nanoindentation information as a function of diffusible as well as trapped hydrogen by varying the hydrogen charging and nanoindentation sequences. In addition, the cell enables the investigation of hydrogen permeation behavior on the sample surface using the Kelvin probe-based potentiometric hydrogen electrode technique, see [22]. This technique validates the presence and permeation behavior of hydrogen on the sample surface by measuring the variation on the chemical potential. In particular, we used alloys with different substitutional elements (Cr and Al), different Cr contents and different grain orientations for this study. Furthermore, a more comprehensive understanding of the changes in the mechanical response of the materials used due to hydrogen is achieved by complementing different post-mortem characterization methods. Particularly, in this work, we begin to fully exploit the method to study the dynamic effect of hydrogen charging on mechanical properties. We present novel

nanoindentation data as a function of time and hydrogen charging conditions that correlates with the hydrogen diffusion behavior during the transient periods of hydrogen charging and release. Finally, we present a distinct tendency of hydrogen content and a corresponding linear increase in hardness in two regimes where the slope is composition and grain orientation dependent.

2. Experimental procedure

2.1. Materials and sample preparation

Table 1 shows the chemical composition of the investigated Fe-15.9 at.% Cr, Fe-21.2 at.% Cr and Fe-4.4 at.% Al ferritic alloys, hereafter named Fe-16Cr, Fe-21Cr and Fe-4Al, respectively. The FeCr alloys were hover melted, cast to a Cu mold, hot rolled to a thickness of 4 mm at 1100 °C, followed by homogenization annealing at 1300 °C for 4 h in an Argon atmosphere, quenched in water and finally annealed at 800 °C for 1 h with water quenching for grain growth. Fe-4Al was used as reference material with the lowest content of the substitutional element. 4 at.% of Al was added to stabilize the bcc structure. The Fe-4Al alloy, which consisted of a bicrystal with a Σ5 (3 1 0)[0 0 1] grain boundary, was grown using an in-house modified Bridgman technique, see details on material preparation and microstructure characterization in [23]. All the alloys were cut into 2.4 mm thick disks of 12.4 mm diameter by electrical discharge machining. The samples were wet ground sequentially using 1000–4000 grit SiC papers and then mechanically polished with diamond suspension up to 1 μm. Before final polishing with a 40 nm colloidal silica suspension for 1 h, the samples were etched with a V_2A agent for 10 s to remove the remaining deformation layer.

2.2. Microstructure characterization

The final surface roughness was measured by atomic force microscopy (AFM, Dimension™ 3000), and the resulting root mean square was < 1 nm over 1 μm^2, analyzed using Gwyddion. The dislocation density (<10^{13} m^{-2}) was measured by electron channeling contrast imaging (ECCI) in a field-emission scanning electron microscope (SEM, Carl Zeiss AG, Crossbeam, Germany) at an accelerating voltage of 30 kV, a beam current of 4nA, and a working distance of 7–7.5 mm. Most residual carbon forms carbides along grain boundaries while oxygen forms large chromium oxides of ∼ 4 μm in diameter (see Supplemental Material Fig. S1). These microstructural features were avoided during the measurements. All the specimens were polished right before conducting the experiments to eliminate the influence of grown oxide layers other than the native oxides.

Electron backscatter diffraction (EBSD, Jeol, JSM 6490) was used to confirm the presence of a single bcc phase and to obtain the crystallographic orientation of each grain to be tested (as the example for Fe-16Cr of Fig. 1a and Fig. S2). The displayed image represents EBSD maps acquired using a combo-scanning technique that combines several individual maps over a few millimeters to cover a large area. The slight color variation observed within one grain in the image originates from minor shifts that occur when the stage position changes during the combo EBSD scanning. Normal direction-inverse pole figure (ND-IPF) maps were created with the TSL software. Three defined grain orientations were chosen in Fe-21Cr as shown in Fig. 1a, and Fig. S2 with orientation deviations < 8° to (1 0 0), (1 1 0) and (1 1 1) (i.e. [0 0 1], [1 1 0], [1 1 1]//ND, respectively). To compare the effect of substitutional elements within the same grain orientation, the (1 0 0) orientation was selected also for Fe-16Cr and Fe-4Al. For simplicity, only Miller indices are used hereafter. The measured Euler angles (φ1, Φ, φ2) of the chosen grains are listed in the Supplemental Material (Table S1). These ND orientations are also the loading directions for nanoindentation. The average grain size was ∼ 1.2 mm for the Fe-Cr alloys, large enough for performing all tests under different charging conditions within a single grain. Transmission electron microscopy (TEM) foils of the cross-section underneath the nanoindentation imprints were lifted out using a dual-beam focused Ga-ion beam (FIB, FEI, Helios 600i) instrument operating at 30 kV. The TEM foils were cleaned by Ga-ion beam with 2 kV 27 pA for 5 min prior to TEM studies. Bright-field (BF) scanning transmission electron microscopy (STEM) observations, including the dislocation analysis, were carried out at 200 kV using a TEM (Jeol, JEM 2200FS) equipped with an omega energy filter. Unfiltered and low-loss energy-filtered images with a slot width of ∼ 20 eV were collected to determine the TEM foil thickness using the log-ratio method [24]. Crystallographic analysis and foil thickness measurements were conducted using the platform Fiji [25].

2.3. Nanoindentation

Nanoindentation was performed in a load controlled G200 instrument (former Agilent, currently KLA) for a maximum load of 10 mN with a Berkovich diamond indenter. The continuous stiffness measurement (CSM) method was applied at a constant strain rate of 0.1 s^{-1} with a frequency of 45 Hz and harmonic displacement of 2 nm [26]. The hardness and elastic modulus of the alloys were extracted based on the Oliver and Pharr's theory at an indentation depth of 250–350 nm to avoid the indentation size effect [27]. A Poisson's ratio of 0.3 was assumed in this study as commonly used for steels [28]. A 5 s holding time at the maximum load was applied to eliminate the effect from creep properties for the unloading curve. The 60 s holding period at 10 % of the peak load following the unloading segment determined the thermal displacement and can be used to compensate for the system's thermal expansion or contraction [29].

2.4. Electrochemical hydrogen charging

The *in situ* electrochemical backside hydrogen charging setup, consisting of a three-electrode cell, was mounted inside the nanoindentation chamber. Details of the cell are elucidated in [22]. The setup body was manufactured in Polychlorotrifluoroethylene (PCTFE), with high stiffness and a low water absorption rate. The 0.1 M NaOH solution with an addition of 20 mg/L As_2O_3 to inhibit the hydrogen recombination reaction was mixed with 10 wt% of Agar at 50 °C to prepare the electrolyte in a hydrogel form [22]. A steady Ar flow with a rate of 3.5 L/min was introduced

Table 1
Chemical composition of the materials investigated (in at.%). (Note the sample names Fe-16Cr, Fe-21Cr and Fe-4Al refer to at %.).

Element	Fe	Cr	Al	C	O	P	S	Si
Fe-16Cr	83.973	15.922	0.002	0.010	0.072	0.004	0.007	0.010
Fe-21Cr	78.786	21.158	0.002	0.014	0.041	0.004	0.004	0.010
Fe-4Al	95.290	0.009	4.420	0.043	0.228	0.004	0.001	0.005

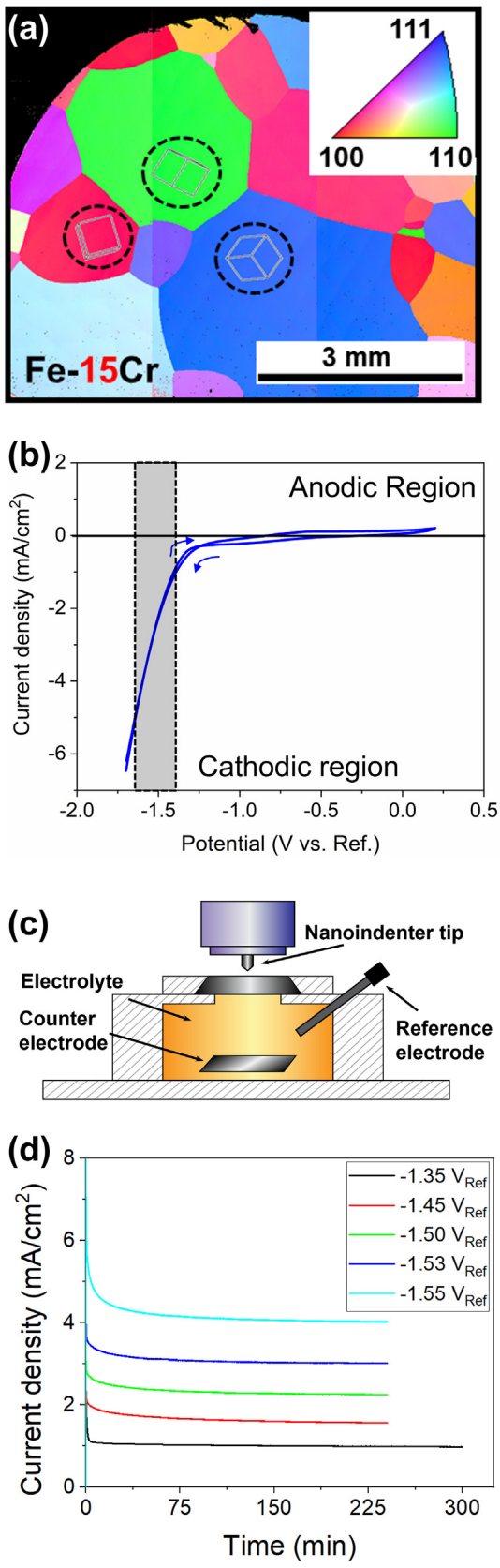

Fig. 1. (a) Representative EBSD ND-IPF map of Fe-16Cr showing a homogeneous ferritic structure with a mean grain size above 1 mm. (b) Example of a cyclic voltammetry curve highlighting the current density region of −1 to −5 mA/cm^2 where HER is promoted in this work. (c) Schematic of the in-situ backside hydrogen electrochemical charging setup (reproduced from [22]). (d) Evolution of current density during potentiostatic charging at different cathodic potentials.

into the chamber to reduce the oxygen content and diminish the release of hydrogen.

Cyclic sweep voltammetry tests with a scanning rate of 50 mV/s from −1.7 V to 0.3 V were conducted by a Reference 600™ Potentiostat (Gamry Instruments). All the electrochemical potentials were recorded with respect to the reference electrode as V_{Ref}. The potentials were chosen to achieve current densities between −0.5 to −5.5 mA/cm^2 (as indicated by the grey region in Fig. 1b), promoting the hydrogen evolution reaction (HER) while preventing excessive hydrogen bubbles. Within this range, there exists a proportional relationship between the applied potential and the current density [30,31]. The experimental setup is schematically displayed in Fig. 1c. The electrolyte contact area with the specimens is a circular region with a diameter of 8 mm. Fig. 1d shows that the current density was able to remain constant for more than 300 min during potentiostatic charging. Either the increase of current density or charging time can be expected to produce a higher amount of hydrogen within the alloy [32]. This proportional relationship between the cathodic current density and hydrogen activity was also observed at room temperature by Dafft et al. in pure iron with a current density below 5 mA/cm^2 [33] and by Marchetti et al. in 9 %Cr-1 %Mo steels with a current density range of 0.1–10 mA/cm^2 [34], similar to our experimental conditions.

2.5. In situ electrochemical backside hydrogen charging during nanoindentation

Each hydrogen charging experiment was composed of four segments: pre-charging, reference, *in situ* charging and hydrogen release. The initial conditions were set on the knowledge of the diffusion coefficient of the Fe-21Cr alloy by preliminary tests shown in [22] which also proved the hydrogen presence on the upper, nanoindentation side. Once the cell was filled with the electrolyte and mounted in the nanoindenter chamber, a pre-charging cycle with a current density of 2 mA/cm^2 for 3 h was applied to fill deep hydrogen traps (these conditions were determined after several tests). Subsequent release of the diffusive and lightly trapped hydrogen was achieved by turning off the applied potential for at least 6 h. After this time, a series of indentations were performed to collect the reference mechanical properties of the sample mounted in the filled cell. Hereafter, the reference data, without hydrogen, refers to the condition after pre-charging when all the deep traps are filled but the diffusive and lightly trapped hydrogen was released. The hardness before pre-charging was also investigated and its variation with respect to the hardness after the hydrogen pre-charging/release cycle is<1.5 %, well within the measurement error bar. Afterwards, the *in situ* hydrogen charging segment began with a stepwise increase of the potential and continuous monitoring of the current density. Each step lasted for at least 4 h as shown in the results section. Finally, hydrogen charging was ceased and hydrogen was released from the alloys at ambient temperature. The mechanical data by nanoindentation were collected continuously and simultaneously during the whole procedure, starting with the reference data, during hydrogen charging and ending after 6 h of hydrogen release. It is expected that some deeply trapped hydrogen remains in the sample after 6 h. However, no changes in the mechanical data were detected after this time.

3. Results and interpretation

3.1. Influence of hydrogen on the mechanical properties

Reference (black) and during hydrogen exposure (red), load–displacement representative curves for Fe-4Al (100), Fe-16Cr

(100) and Fe-21Cr (100) are shown in Fig. 2a, b and c, respectively. Hardness and Young's modulus were averaged at depth values between 250 and 350 nm, highlighted by the grey area and magnified in the corresponding insets. The top curves in Fig. 2d-f show the hardness (red) and Young's modulus (blue) evolution as a function of time. Each dot corresponds to a single nanoindentation test with a time resolution of ~ 5 min. The bottom curves (green) show the corresponding average current density recorded during potentiostatic hydrogen charging at a given potential (examples of these curves were given in Fig. 1d).

A gradually increased hardness due to hydrogen is visible in the three studied alloys. This increase starts soon after the applied cathodic potential for hydrogen charging is changed, since the breakthrough time for hydrogen permeation in these alloys is in the order of<10 min, according to [22]. During the first hydrogen charging stage, the hardness increased following a sigmoidal shape that correlates with the hydrogen diffusion behavior and stabilized in a plateau at which the dynamic equilibrium state of the absorbed and desorbed hydrogen permeation flux is reached. Because of the Fe-base bcc structure with high hydrogen diffusivity in the order of 10^{-10} m^2/s [22], the difference in the diffusion coefficient between the three studied alloys is expected to be minor. To consider these differences in the diffusion behavior during the initial charging, the averaged hardness and Young's modulus shown hereafter in Fig. 4 are thus collected after hydrogen distributes homogeneously in the sample surface (i.e. when reaching the hardness plateau). The hardness plateau contains more than 20 data points for each polarization condition. Stabilizing the hardness values upon hydrogen release requires about 60 % longer time than hydrogen charging. The hardness value takes ~ 2.6 h to reach the first plateau for the Fe-16Cr alloy; this time varies depending on the composition (Fig. 2e). A longer duration of ~ 4.2 h is required for hydrogen release from the specimen until the hardness drops back to the initial reference value once the charging procedure is stopped. The longer duration for hydrogen releasing can be explained by a slower release of hydrogen from flat trapping sites and deeply trapped hydrogen. It is noteworthy that during the final hydrogen release stage, when the hydrogen charging process is ceased, the hardness values gradually return to the original values over time (Fig. 2d-f), indicating that the entire hardness increase can be attributed to the presence of diffusive hydrogen.

The Fe-4Al (100) alloy in Fig. 2d shows that during the first hydrogen charging stage, with a current density of 0.93 ± 0.04 m A/cm^2, the hardness turns to a constant value of 2.19 ± 0.03 GPa. Compared with the reference condition of 2.10 ± 0.03 GPa without hydrogen, the hardness increased by 4.3 %. The hardness rises only to 2.20 ± 0.04 GPa (4.7 % rise) when the charging current density reaches the maximum value of 5.21 ± 0.03 mA/cm^2, which shows that an increased hydrogen supply does not strongly affect further the mechanical behavior and that the effect of hydrogen is small in the Fe-4Al alloy. The measured Young's modulus stays unchanged considering the error bars, with 206 ± 2 GPa for the reference state and 209 ± 3 GPa for the hydrogen charged conditions (Fig. 2d). Similar behaviors are observed for the Fe-Cr alloys. For Fe-16Cr (100) (Fig. 2e), the hardness increases from the reference condition 2.17 ± 0.02 GPa to 2.42 ± 0.02 GPa (11.5 % enhancement) during charging with the highest current density used of 4.21 ± 0.05 mA/cm^2. In contrast to the hardness, Young's modulus remains constant with values of 208 ± 3 GPa (reference state) and 205 ± 2 GPa (during hydrogen charging). The most pronounced hardening effect is observed in Fe-21Cr (100), where the hardness increases by 17.8 %, from 2.43 ± 0.03 GPa in the reference state to 2.86 ± 0.02 GPa by applying a potential of −1.58 V_{Ref}, that corresponds to a current density of 4.66 ± 0.02 mA/cm^2 (Fig. 2f). Again, the Young's modulus remains invariable at 208 ± 2 GPa. The highest current densities used were determined experimentally for the

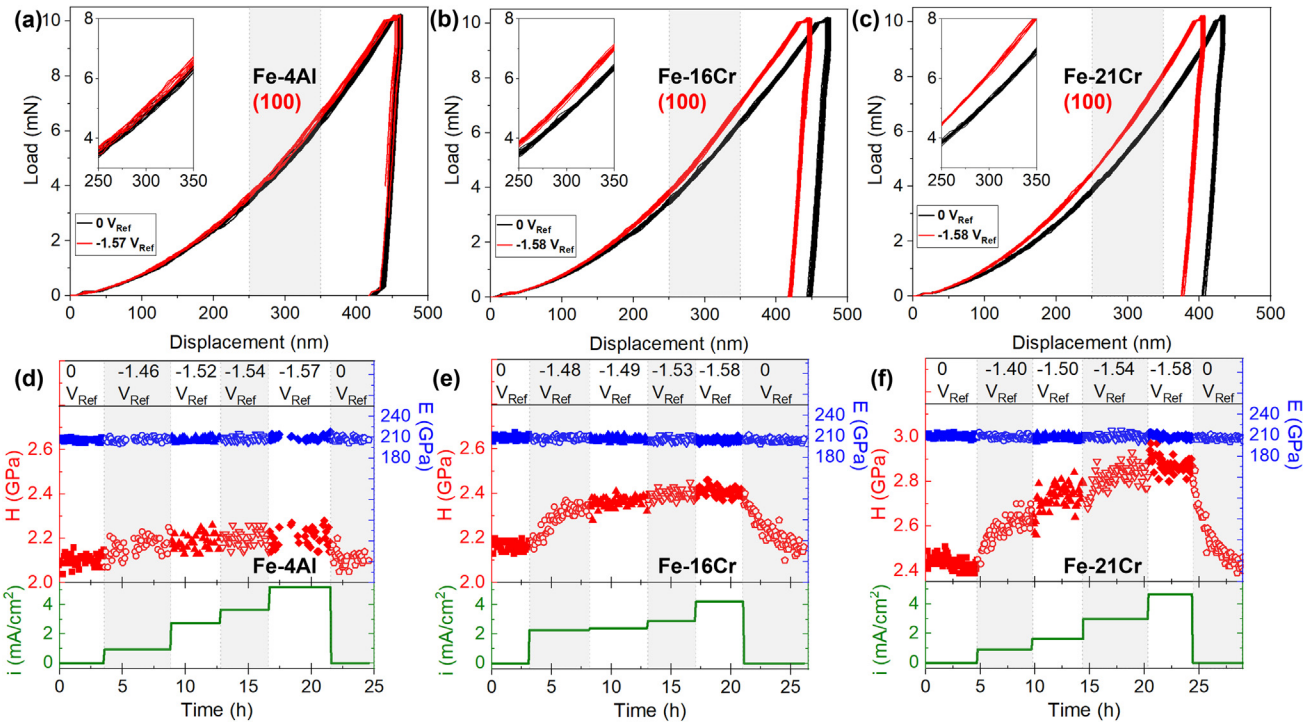

Fig. 2. Representative nanoindentation load–displacement curves of reference data (black) and during hydrogen charging (red) at the specified potential for (a) Fe-4Al (100) a, (b) Fe-16Cr (100)b and (c) Fe-21Cr (100)c. Labels a, b and c after the grain orientations refer to specific grains presented in Fig. 4 and Table S1. Hardness (red) and Young's modulus (blue) evolution and average current density (green) measured for different potentials in (d) Fe-4Al, (e) Fe-16Cr and (f) Fe-21Cr. Different symbols in the hardness and Young's modulus data represent different charging potentials. (For interpretation of the references to color in this figure legend, the reader is referred to the web version of this article.)

different alloys. Current densities above 5 mA/cm^2 were also attempted. However, they result in an uncontrolled hydrogen production at the metal/liquid interface, for the studied alloys here are not completely absorbed in the material (bcc Fe alloys can only absorb a small quantity of hydrogen). The hydrogen excess is therefore recombined as H_2 and forms bubbles that disturb the mechanical data in the form of vibrations. Moreover, these bubbles reduce the contact area of the electrolyte with the interface, therefore resulting rather detrimental to the experimental procedures.

The hydrogen effect on different grain orientations is investigated by applying the same hydrogen charging procedure to Fe-21Cr with different grain orientations of (100), (110) and (111), respectively in Fig. 3a-c; note that the range of hardness variation is the same for the three figures. Data for Fe-21Cr (100) (Fig. 3a) is the same as in Fig. 2f. Regarding the Fe-21Cr (110) alloy (Fig. 3b), the hardness enhanced from the initial 2.74 ± 0.02 GPa to 3.13 ± 0.02 GPa at a current density of 4.18 ± 0.02 mA/cm^2 (14.2 % increase) and the Young's modulus remains constant at 224 ± 2 GPa. For (111) orientation of Fe-21Cr (Fig. 3c), an increase in hardness from 2.59 ± 0.03 GPa without hydrogen charging to 2.99 ± 0.03 GPa is achieved by charging at a current density of 4.04 ± 0.02 mA/cm^2 (15.5 % rise in hardness).

Fig. 4 summarizes the data of the three alloys, including different grain orientations. For all cases, the elastic modulus remains constant with a maximum deviation of 1.7 % (Fig. 4a), which is within the accuracy of the measurements. The corresponding symbols for the specific three conditions displayed in Fig. 2d-f are circled with solid black lines in Fig. 4b. Fig. 4b shows the hardening effect obtained in (100) oriented grains for Fe-4Al, Fe-16Cr and Fe-21Cr during hydrogen charging. ΔH is defined as $\Delta H = H_i - H_0$, with H_i being the hardness at a given current density and H_0 the reference hardness without hydrogen charging. ΔH is analyzed to solely investigate the hydrogen introduced effect, in avoidance of the influence from substitutional element content and the grain orientations. The hardness initially increases linearly upon increasing the current density, corresponding to a higher amount of hydrogen introduced into the samples. There exists a turning point for the increasing tendency with applied current density between the range of 2–3 mA/cm^2, above which the slope of the absolute hardness experiences a drastic decrease, indicating an establishment of a quasi-equilibrium state for introduced and released hydrogen flux. An increase of flow stress was also shown experimentally in Fe-17wt.%Cr steel at room temperature by a tensile test conducted on an electrochemically charged sample [35]. Additionally, the material with a higher Cr content exhibits a higher hardening effect with the same current density applied. The magnitude of the hydrogen effect for different alloy compositions can be compared by calculating the slope of the initial linear increase in hardness with increasing charging current density with units of GPa/(mA·cm^{-2}). With the grain orientation of (100), the slope of Fe-21Cr for the first stage ($k(1)_{Fe\text{-}21Cr}$) is 0.178 ± 0.006, which is almost twice the value of Fe-16Cr ($k(1)_{Fe\text{-}16Cr}$) that is 0.079 ± 0.004. Above the transient region of 2–3 mA/cm^2, the second stage slope approaches a similar value of 0.014 ± 0.003 ($k(2)_{Fe\text{-}21Cr}$) and 0.015 ± 0.003 ($k(2)_{Fe\text{-}16Cr}$) in Fe-21Cr and Fe-16Cr, respectively. Although only a couple of values could be collected for Fe-4Al, the $k(2)_{Fe\text{-}4Al}$ can be calculated as 0.005 ± 0.002. The increase in hardness change (ΔH) when charged with hydrogen above the turning region (greater than2–3 mA/cm^2) at 3 mA/cm^2 based on Fig. 4b for Fe-4Al, Fe-16Cr and Fe-21Cr with (100) grain orientation was calculated from the fitting curves. Fe-21Cr possesses the highest enhancement of 16.7 ± 0.3 %, while Fe-4Al has the lowest increase of 4.3 ± 0.1 %. The intermediate incremental of hardness occurs in Fe-16Cr with 10.8 ± 0.1 % increase.

The anisotropy on the hydrogen-induced hardening effect for different grain orientations of (100), (110) and (111) was investigated for the Fe-21Cr alloy (Fig. 4c). The initial slope of the (100) grain has the highest value of 0.178 ± 0.006, while the (111) grain owns the lowest slope of 0.133 ± 0.008, with an intermediate value for the (110) grain of 0.152 ± 0.001.

3.2. Influence of hydrogen on the microstructure beneath the imprint

Since an advantage of the backside charging setup is that the top surface of the specimen used for indentation testing stays pristine even after hydrogen charging, the change in hardness must be reflected by the deformation structure underneath the indent. Here, pristine means free from the influence of effects other than hydrogen, such as surface contamination due to the elements contained in the electrolyte in contact with the surface, as well as increased surface roughness and possible corrosion caused by other hydrogen charging methods. Therefore, the front surface roughness of Fe-21Cr before and after hydrogen charging stays unaltered (<1 nm/μm^2 on average) as measured by atomic force microscopy in Duarte et al. [22]. The chemical composition of the specimen before and after the hydrogen charging has been investigated by X-ray photoelectron spectroscopy (XPS), as shown in the supplemental material Fig. S3. These data show that the chemical composition of the indented surface after backside hydrogen charging remains the same as the reference (uncharged) surface, consisting of a native oxide layer of about 4 nm. However, the bottom surface in contact with the electrolyte shows an increased oxide layer with a thickness of 8 nm and higher Cr content while Fe is depleted.

A representative condition was chosen for further microstructural analysis as the hydrogen-induced hardening effect is found in all different materials. FIB cross-sections were extracted from the residual nanoindentation imprints and analyzed by BF-STEM. Fig. 5a and b show the dislocation structure after indentation in the hydrogen-free and hydrogen-charged Fe-21Cr samples within

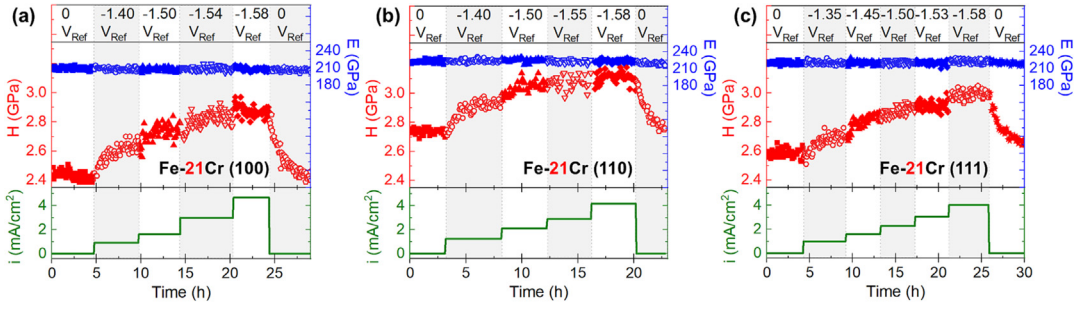

Fig. 3. Hardness (red) and Young's modulus (blue) evolution and average current density (green) for different potentials in Fe-21Cr with different grain orientations of (a) (100), (b) (110) and (c) (111). Different symbols in the hardness and Young's modulus data represent different charging potentials. (For interpretation of the references to color in this figure legend, the reader is referred to the web version of this article.)

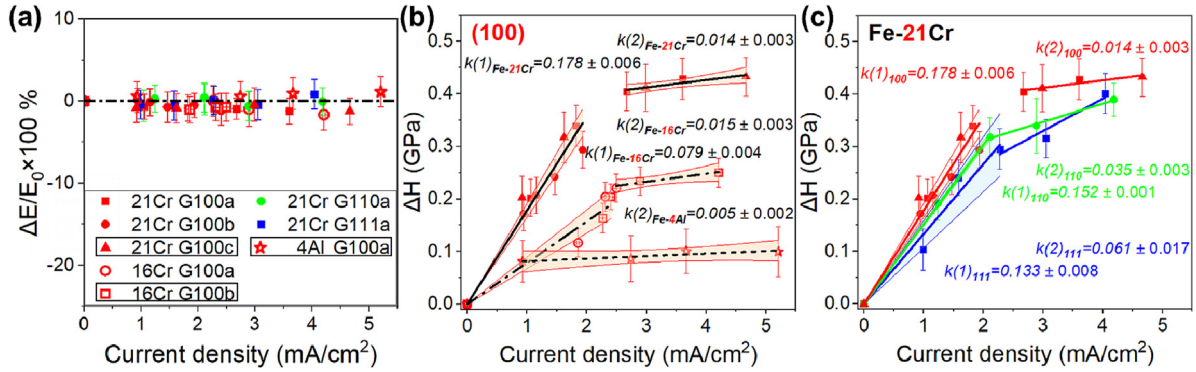

Fig. 4. (a) Relative variation of Young's modulus, $\Delta E = E_i - E_0$, normalized by the reference value E_0 of the hydrogen-free Fe-4Al, Fe-16Cr and Fe-21Cr samples. Different numbers indicate different grain orientations: G100 are (100) oriented grains (red data points), G110 (110) (green), and G111 are (111) grains (blue). For each orientation, up to three grains were measured, indicated by the letters a, b and c. The data highlighted here in black rectangles correspond to the three hardness evolution curves shown in Fig. 2d-f. (b) Comparison of hardness variation, $\Delta H = H_i - H_0$, of the hydrogen-free Fe-4Al, Fe-16Cr and Fe-21Cr samples within the same (100) grain orientation. (c) ΔH evolution tendency in three grain orientations of (100), (110) and (111) for Fe-21Cr. k denotes the slope of the fitting curves with units of GPa/(mA·cm^{-2}), k(1) stands for the initial stage, while k(2) represents the second stage of hardness evolution. The shaded regions represent the 95% confidence bands of the fitted curves. (For interpretation of the references to color in this figure legend, the reader is referred to the web version of this article.)

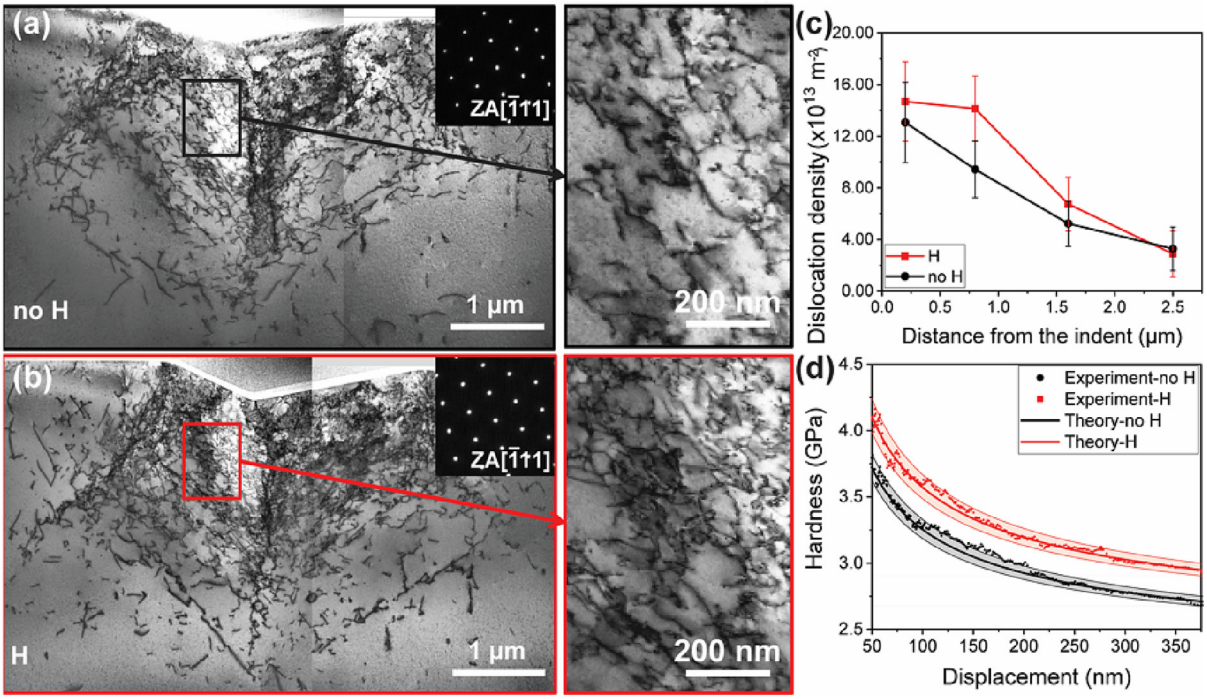

Fig. 5. Representative BF-STEM analysis of the dislocation structure underneath nanoindentation imprints in Fe-21Cr(110) imaged in [−111] zone axis (ZA): (a) Without hydrogen; (b) Post-mortem after charging with a current density of 2.11 mA/cm^2 at −1.5 V_{Ref} during nanoindentation. (c) Comparison of dislocation density with and without hydrogen. (d) Experimental and theoretical hardness curves with respect to the indentation depth based on Eq. (6) and (7) for the sample with and without hydrogen, respectively. The shaded regions represent the error band by considering the errors originating from the plastic zone.

(110) orientation, respectively. The hydrogen charged sample was indented while exposed to a current density of 2.11 mA/cm^2 at −1.5 V_{Ref}. A comparison of Fig. 5a and b reveals a higher dislocation density for the hydrogen charged sample in the vicinity of the imprints, as quantitatively displayed in Fig. 5c. The difference in dislocation density between the hydrogen charged and the reference samples without hydrogen charging decreases with increased distance from the indent as few dislocations exist in the material matrix. Details on the calculations of the dislocation density and thickness of the TEM foil are found in the Supplemental Material (Fig. S4). Throughout the plastic zone, an increase in dislocation density of 24 % is observed in the presence of hydrogen ($\rho_{dis,\ H} = 9.6 \times 10^{13}$ m^{-2}) compared to the hydrogen-free reference ($\rho_{dis,\ noH} = 7.8 \times 10^{13}$ m^{-2}). The following formula was used to calculate the dislocation density:

$$\rho_{dis} = \frac{l}{t_f \times A} \tag{1}$$

where ρ_{dis} is the dislocation density, l is the total length of dislocations measured by image filtering, A is the evaluated area, t_f is the thickness of TEM foil.

A high density of tangled dislocations was also found in TEM by Wang et al. after cathodically charging pure Fe while conducting a stress relaxation test [36]. In our post-mortem dislocation analysis, we observe that the difference in dislocation density becomes less pronounced with increasing the distance from the indent.

4. Discussion

4.1. Hardening effect of principal substitutional elements

The higher hardness for the FeCr alloy with 21 at.% Cr compared to 16 at.%Cr can be attributed to substitutional solid solution strengthening (Fig. 4b). The larger atomic radius of Cr creates a strain field around Fe atoms interacting with dislocations [37–39]. By characterization upon *in situ* TEM with Fe-14 wt.%Cr (95–300 K), Caillard [40] reported that the screw dislocation mobility is strongly affected by the local pinning of solute at superjogs, causing the solid solution hardening. Matijasevic and Almazouzi [41] report in their studies a linear increase of yield stress with increased Cr content, which fits well to our hardness observation.

4.2. Diffusive hydrogen-induced hardening mechanism

We followed the formalism of Wang et al. [18] to further unravel the hardening effect of hydrogen in Fe-21Cr. However, we employed largely experimental nanoindentation, EBSD, ECCI and TEM data in the calculations shown, which can be easily accessible in our case by the use of the backside charging approach. Based on the Tabor's model, the elastoplastic range of the CSM hardness curve is interpreted by Durst et al. as $H_0 = C\sigma$ [42]. H_0 represents the hardness obtained from indentation tests and C is the Tabor's factor assumed to be 3 in this case to simplify the nanoindentation complex stress state to uniaxial stress state [43]. As the indentation was conducted within a single crystal, the contribution of grain boundaries is not considered, and σ can be interpreted by the contribution of the Taylor's stress (σ_{Taylor}) and the lattice friction (σ_{Fric}), which play an essential role in bcc materials [44], resulting in $\sigma = \sigma_{Taylor} + \sigma_{Fric}$. The hardness H_0 can be therefore expanded as [45]:

$$H_0 = C(\sigma_{Taylor} + \sigma_{Fric}) = C(M\alpha Gb\sqrt{\rho_{dis}} + \sigma_{Fric}) \quad (2)$$

where M is the Taylor factor, which is 3.06 averaged for different grains in bcc materials [46–48], α is an empirical constant depending on the dislocation structure, taken here as 0.22 [42,49]. The shear stress G used is 83 GPa, conjectured from α-Fe studies [50].

The dislocation density ($\rho_{dis} = \rho_{GND} + \rho_{SSD}$) contains both statistically stored dislocations (SSD) and geometrically necessary dislocations (GND). Since the specimen was long time annealed and without pre-deformation, it is reasonable to assume that the dislocation density of 2.4×10^{12} m^{-2} measured by ECCI (Fig. S5) is closely related to the ρ_{SSD} for our material [18]. ρ_{SSD} can be then calculated in this case according to the Nix-Gao model [45]:

$$\rho_{GND} = \frac{3}{2}\frac{\tan^2\theta}{f^3 bh} \quad (3)$$

where θ is 24.63° for the Berkovich tip adapted from literature [18], f is the ratio between the radius of the plastic zone and the contact area, calculated based on the ECCI images of Fe-21Cr (the details are shown in the Supplemental Material Fig. S6). Without hydrogen, the calculated f_{noH} is 2.82 ± 0.12 and 2.57 ± 0.12 for the hydrogen charged sample (f_H). The decreased f value that indicates a contraction of the plastic zone by the introduction of hydrogen was also observed by Wang et al. [18], implying that hydrogen dragged the dislocation motion. The Burger's vector b = 1/2[1 1 1] for the bcc lattice was calculated as 0.222 nm, considering a lattice constant a_0 = 0.256 nm (details shown in the Supplemental Material Fig. S4c-d). In the current experiments, it is feasible to assume that hydrogen influences only the ρ_{GND} and σ_{Fric} as no other features were introduced affecting the ρ_{SSD} by the backside hydrogen charging method. By combing Eq. (2–3), the hardness in the absence and in the presence of hydrogen can be then described as follows in Eq. (4) and (5), respectively:

$$H_0 = C(\sigma_{Taylor} + \sigma_{Fric}) = C(M\alpha Gb\sqrt{\rho_{SSD} + \frac{3}{2}\frac{\tan^2\theta}{f^3 bh}} + \sigma_{Fric}) \quad (4)$$

$$H_0 = C(\sigma_{Taylor} + \sigma_{Fric}) = C(M\alpha Gb\sqrt{\rho_{SSD} + \frac{3}{2}\frac{\tan^2\theta}{f_H^3 bh}} + \sigma_{Fric} + \sigma_H) \quad (5)$$

The measured and theoretical fitted curves with and without hydrogen are shown in Fig. 5d. The lattice friction stress in the absence of hydrogen is deduced as 710 MPa from Eq. (4), and it is close to the 678 MPa value obtained in a Fe-12 wt.%Cr alloy by considering solid solution strengthening in [41]. The difference might arise from the evaluation of the plastic zone in the ECCI image and differences in the alloy composition. However, this does not affect the relative calculated stress contribution by hydrogen. Based on Eq. (5), the contribution of hydrogen to the overall stress σ_H. was calculated as 50 MPa, which is attributed to the interaction of hydrogen with dislocations. Due to the high hydrogen diffusivity in bcc alloys [4] and the deep trapping site for hydrogen that constitutes the dislocation core [7,51], it is expected that the local accumulation of hydrogen in the high-stress region beneath the indenter is sufficient to form a Cottrell atmosphere, which can drag the moving dislocations rather than accelerate the dislocation motion. This pinning/dragging impedes the movement or cross-slip of dislocations, leading to strain hardening [52,53], which is consistent with the solute drag theory and supported by atomistic simulations in α-Fe [54,55]. Particularly in bcc alloys, the formation and movement of kink pairs at screw dislocations are critical in determining the plastic behavior at a temperature below 340 K [56]. When kink motion is the rate-controlling step, the increase of lattice friction might be ascribed to the interaction of hydrogen solute atoms that segregate to the kinks and inhibit their motion according to simulations [17]. Besides, hydrogen facilitates vacancy generation, which retards the dislocation motion as well. Most *ex situ* experiments cannot eliminate the effect from trapped hydrogen. In our case, the reference data was taken after the pre-charging procedure filling the deep traps. Therefore, the observed hardening effect is due to the diffusive hydrogen and hydrogen trapped by flat trapping sites such as dislocations and substitutional elements causing lattice distortion [4].

The increase in dislocation density with hydrogen, as observed in Fig. 5c, can be calculated as the ratio of f_H^3/f_{noH}^3. As ρ_{SSD} is one order of magnitude smaller than ρ_{dis}, and similar for the charged and uncharged states, thus ρ_{GND} approximately equals to ρ_{dis}. The ratio of the dislocation density for the uncharged ($\rho_{dis,\ noH}$) and charged ($\rho_{dis,\ H}$) sample can be estimated by the following equation:

$$\frac{\rho_{dis,\ noH}}{\rho_{dis,\ H}} \approx \frac{\rho_{GND,\ noH}}{\rho_{GND,\ H}} = \frac{f_H^3}{f_{noH}^3} \quad (6)$$

where $\rho_{GND,\ noH}$ and $\rho_{GND,\ H}$ are the density of GND for the uncharged and charged samples, respectively. The calculated ratio of f_H^3/f_{noH}^3 is 1.32 ± 0.34 and coincides well with the ratio of the dislocation density 1.24, calculated from Fig. 5c. A massive amount of dislocations entangled in the vicinity of the imprint, which might lead to the deviation of the value, especially for the hydrogen charged lamella with a higher amount of dislocations.

This increase in dislocation density with hydrogen can be attributed to reducing the free energy for the dislocation line energy according to the "defactant theory" developed by Kirch-

heim [17]. The "defactant theory" is based on a thermodynamic model [17] and the experimentally observed pop-in reduction phenomenon [18,21,57]. The reduction of the pop-in load was shown in our previous work for the same Fe-21Cr alloy in [22]. These two studies show that the generation and multiplication of dislocations are facilitated in the presence of hydrogen, leading to dislocation entanglement and material strengthening [55]. Besides, multiscale simulations in Ni suggest nano-hydrides formation around the dislocation lines, which can impede dislocation motion [58] – a scenario that is so far experimentally not confirmed. In summary, our results support the interpretation that hydrogen initially facilitates dislocation nucleation following the "defactant theory"; afterwards, Cottrell clouds form and increase the resistance force for dislocation motion according to the solute drag theory [55]. The synergy of both effects results in a drastic enhancement of the hardness observed in the present study, while the modulus remains unaffected.

4.3. Hydrogen-induced hardening effect with the increasing content of principal substitutional elements

Fig. 6 shows the diffusible hydrogen-induced hardening normalized by the hydrogen-free (pre-charged) measurement in Fe-4Al, Fe-16Cr and Fe-21Cr samples with (100) grain orientation. The data corresponds to ~ 3 mA/cm^2 based on Fig. 4b, above the turning point in the hardness behavior. The difference of electronegativity of Cr (0.54) or Al (0.59) to hydrogen is higher than that of Fe to hydrogen (0.37) according to the Pauling scale, which indicates a higher chemical affinity of Cr (or Al) to hydrogen [59]. The increased hydrogen-induced hardening effect can be discerned with the increasing content of Cr and Al in the ferritic alloys. A targeted study is necessary to study the individual effect of each principal substitutional element and therefore we will focus here on the comparison of the Cr containing alloys. Nevertheless, it is crucial to notice that the content of principal substitutional elements plays a critical role in this hardness differentiation in Fig. 6, as the influence of the initial dislocation density and alloy interfaces can be excluded since the experiments were conducted in single grains with low dislocation density as measured by ECCI.

In the Fe-Cr alloys, a more pronounced hydrogen-induced hardening effect can be observed with higher Cr content. Substitutional Cr atoms cause lattice distortions creating a dilational misfit and

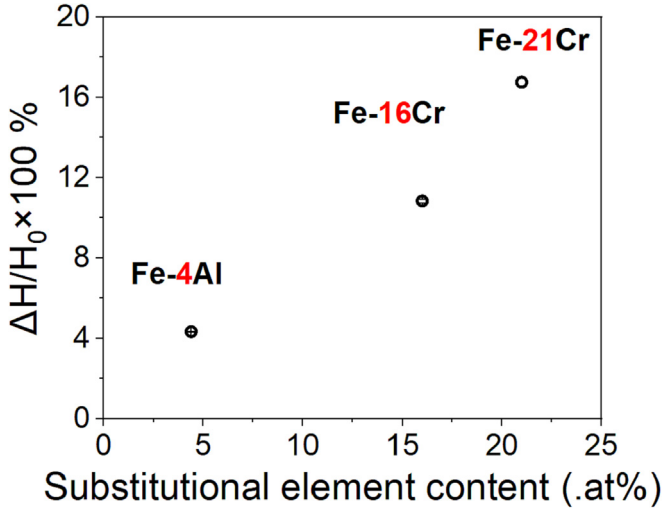

Fig. 6. Relative variation of the hardness normalized by the reference H_0 (hydrogen-free) for Fe-4Al, Fe-16Cr and Fe-21Cr samples as a function of the principal substitutional element content at 3 mA/cm^2 based on Fig. 4b.

therefore more space for hydrogen. According to ab-initio simulation works in α-Fe and Fe-9 wt% Cr by Ramunni et al., substitutional Cr atoms could transverse the stable state of tetrahedral sites in pure Fe to a non-symmetrical state and create a new octahedral site that is more stable for hydrogen to sit in [60]. This introduction of a new octahedral site in the Fe-9 wt% Cr alloy results in a substantial reduction of 200 times in the hydrogen diffusion coefficient from 10^{-4} cm^2/s to 5 × 10^{-7} cm^2/s and a permeation coefficient 10 times lower when compared to pure and annealed α-Fe at 30 °C. This also suggests an increase in hydrogen solubility [60]. Besides, hot extraction chemical analyses show that the hydrogen content in Fe-10.4 wt% Cr is higher than in pure Fe after being immersed in 1 M H_2SO_4 at 25 °C for 25 h [4].

Furthermore, a hydrogen trap with<30 kJ/mol binding energy is generally considered a reversible flat trapping site [4,61]. The dilated sites near dislocations, large atoms of alloying elements and the stress field around precipitates are usually in this category of flat traps. In contrast, dislocation cores, grain boundaries, and interfaces with more than 50 kJ/mol binding energy are treated as deep traps [4]. The binding energy of hydrogen to Cr obtained by simulations in ferritic steels is 26–27 kJ/mol, which corresponds to flat hydrogen trapping sites [4,6,7]. Fe-Cr alloys would then absorb more hydrogen with a higher Cr content, leading to an increase in hardness. This was also observed in α-Fe compared to 13Cr and 16Cr binary alloys [62].

4.4. Anisotropy in hydrogen-induced hardening effect

Fig. 4c displays the anisotropy on the hydrogen-induced hardening effect for different grain orientations of (100), (110) and (111) for Fe-21Cr. When the applied current density is below the turning point of 2–3 mA/cm^2, the initial slope of the (100) grain has the highest value than (110) and (111) grains. This observation coincides well with the density functional theory (DFT) simulations performed in bulk bcc iron that shows hydrogen occupies the deep subsurface tetrahedral sites in (110) instead of the shallow subsurface tetrahedral sites in (100) during the diffusion process [63]. Therefore, a much lower barrier is predicted to exist in (100) than in (110) for hydrogen hopping through the adjacent tetrahedral sites following a curved path. On the contrary, the tendency of the slope for these 3 orientations is opposite above the transient current density region of 2–3 mA/cm^2 ($k(2)_{100}$ < $k(2)_{110}$ < $k(2)_{111}$), which might indicate a faster equilibrium in the (100) orientation. It needs to be noted that the applied current density in this study is limited (<5 mA/cm^2). The anisotropic hardening effect between different grain orientations might not exist with higher applied current density, which requires further research.

4.5. Hydrogen concentration profile

The hydrogen diffusion behavior during hydrogen charging of the studied alloys can be described by the Fick's laws since the influence of deep traps can be excluded. The Fick's 1st law that applies to a steady state system where the concentration keeps constant is:

$$J = -D\frac{dC(x)}{dx} \tag{7}$$

where J represents the diffusion flux (amount of hydrogen passing through per unit area per unit time), D is the diffusion coefficient, and $C(x)$ is the concentration of hydrogen in the specific analyzed position x. However, the hydrogen concentration within the system is changed with time as hydrogen was produced continuously from the backside of the specimen. The one dimensional Fick's 2nd law here is applied to describe this condition:

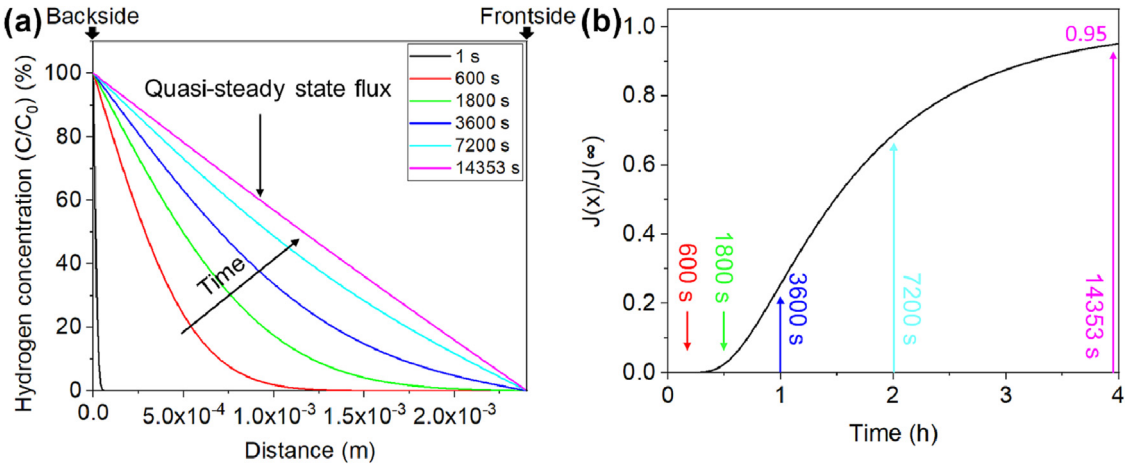

Fig. 7. (a) Modelling of the distribution curves of hydrogen concentration along the specimen depth for different hydrogen charging times in Fe-21Cr. Charging starts at the backside and continues until the system reaches a quasi-steady state (95 % of the steady state of hydrogen reaching the frontside). (b) Simulated evolution curve of the hydrogen permeation flux for different backside charging times.

$$\frac{\partial C(x,t)}{\partial t} = -\frac{\partial J}{\partial x} = D\frac{\partial^2 C(x,t)}{\partial x^2} \tag{8}$$

The frontside of the sample is purged with continuous Argon gas and the hydrogen concentration can be considered 0 all the time (C_2 = 0). For simplicity, the hydrogen concentration at the backside of the sample is considered to be a constant value of C_0 for a given applied current density. The initial bulk hydrogen content is set to 0 ($C(x) = 0$) since the hydrogen concentration is treated as 0 all over the sample before hydrogen charging. Therefore, the initial boundary conditions are given in the following formulas:

$$C_1 = C_0,\ x = 0,\ t \geq 0 \tag{9}$$

$$C_2 = 0,\ x = L,\ t \geq 0 \tag{10}$$

$$C(x) = 0,\ 0 < x < L,\ t = 0 \tag{11}$$

where L is the thickness of the specimen, which is 2.4 mm. This condition inherently assumes a more rapid surface kinetic process than bulk diffusion. The trigonometric solution for the non-steady state of Fick's equation, assuming constant surface hydrogen concentrations, can be obtained by combining it with equations (9–11) [64]. The resulting solution is as follows:

$$\frac{C(x,t)}{C_0} = 1 - \frac{x}{L} - \frac{2}{\pi}\sum_{1}^{\infty}\frac{1}{n}\sin\frac{n\pi x}{L}\exp\left(-\frac{Dn^2\pi^2 t}{L^2}\right) \tag{12}$$

Differentiating Eq. (12) based on Eq. (8), the classic hydrogen flux permeation curve through the sample can be obtained as follows [65]:

$$\frac{J(x)}{J_\infty} = 1 + 2\sum_{1}^{\infty}\cos\frac{n\pi x}{L}\exp\left(-\frac{Dn^2\pi^2 t}{L^2}\right) \tag{13}$$

According to the aforementioned models, the hydrogen concentration distribution curves as a function of time across the specimen are schematically displayed in Fig. 7a. The model is applied to the Fe-21Cr alloy as an example (Fig. 2c). Based on the Kelvin probe-based permeation experiments, the diffusion coefficient used in Fig. 7a and b is 1.5 × 10^{-10} m^2/s for Fe-21Cr [22]. In Fig. 7b, the permeated hydrogen flux on the frontside of the specimen is simulated by Eq. (13). Hydrogen gradually permeates through the specimen when charging continuously from the back side. After a certain duration, the hydrogen flux reaches a steady state set by a constant hydrogen flux $J(\infty)$ permeating through the sample. Infinite duration is required to reach this steady state. Therefore, we collect the hardness values above 95 % of the $J(\infty)$ (14353 s) as the variation afterwards is negligible. The hydrogen flux shows a sigmoidal shape as function of the time, which coincides well with the hardness evolution at the first stage upon hydrogen charging, as exhibited in Fig. 2c, indicating that the hardness variation is attributed to the variation of hydrogen flux in the frontside of the specimen.

4.6. Invariance of Young's modulus with the introduction of hydrogen

A negligible change in the elastic modulus can be found in all the tested alloys during hydrogen charging (Fig. 4a). In fcc Ni [66] and hcp Ti-Mo alloy [67], which can accumulate a more massive amount of hydrogen, a reduction of the elastic modulus was observed, caused by a hydrogen-related lattice expansion. Besides, the elastic modulus reduction might be attributed in some cases to the artificial influence on the test setup or pileup formation as found experimentally [21]. In our case, PCTFE avoids the electrolyte absorption into the charging cell, which guarantees the stability of the setup. In addition, Fischer et al. presented a minor Young's modulus variation in single-crystal bcc Ta where ~ 61 wt ppm of hydrogen reduces 0.08 % of $\Delta E/E$ at ambient temperature [68]. Nonetheless, the hydrogen solubility in bcc is extremely low, with only 0.085 wt ppm diffusible hydrogen contained in Armco iron at ambient temperature [69]. Therefore, the concentration of hydrogen is far from reaching the amount necessary to influence the elastic modulus as claimed by Zhang et al. [70] that hydrogen up to 8 wt ppm does not change Young's modulus in α-Fe at room temperature.

5. Summary and conclusions

We have performed novel *in situ* back side nanoindentation tests on ferritic Fe-4Al, Fe-16Cr and Fe-21Cr alloys to investigate their mechanical response to electrochemically charged hydrogen. The results are summarized below:

- Time-dependent nanoindentation measurements as a function of increased hydrogen supply, correlated to an increased current density/potential applied stepwise, using a backside charging approach is a reliable method to study HE and allow distinguishing between the effects of deeply trapped hydrogen and mobile hydrogen.

- The specific dynamic tendency in the mechanical behavior is shown for the initial transient charging stage and the hydrogen release. Once the charging process starts, the increase in hardness follows the sigmoidal curve corresponding to the diffusion behavior of hydrogen. The hydrogen release stage, after the charging is stopped, requires more than double the time than charging as it includes the release of hydrogen from deeper traps.
- A hardening effect appears in Fe-4Al, Fe-16Cr and Fe-21Cr alloys during hydrogen charging. For low hydrogen content, corresponding to the lower current densities, the hardness variation with respect to the reference hardness follows an initial linear increment with increasing the current density (hydrogen content). There exists a turning point for the increasing tendency with applied current density between 2 and 3 mA/cm^2. Above this value, the slope of the measured hardness variation experiences a drastic decrease, indicating the establishment of a quasi-equilibrium state for the introduced and released hydrogen flux.
- A more pronounced hydrogen-induced hardening effect is observed with a higher concentration of substitutional elements: 16.7 % enhancement in Fe-21Cr, 10.8 % in Fe-16Cr, and 4.3 % in Fe-4Al with a specific current density above the transient region of 2–3 mA/cm^2.
- Anisotropic hardness variation during hydrogen charging within different grain orientations of (100), (110), and (111) is noticed in Fe-21Cr alloy.
- A 24 % increase in the dislocation density is observed by STEM for indents performed during hydrogen charging compared to the uncharged reference in Fe-21Cr.
- The hardening effect is associated with an increased dislocation density beneath the indenter due to hydrogen, and the hydrogen increased stress of $\sim$ 50 MPa.
- The Young's modulus remains constant as the hydrogen solubility in all three bcc alloys is extremely low.

The measurements reveal that diffusible hydrogen impacts dislocation plasticity most. In contrast, trapped hydrogen does not manifest itself in a pronounced hardness change, considering that deep traps did not release all hydrogen at ambient temperature in the air even after a long time in our studies. It can be speculated that adding more deep traps to materials only helps when exposed to a certain amount of hydrogen, as the diffusible hydrogen controls the enhanced hydrogen plasticity. As higher Cr content results in a higher hydrogen hardening effect, it is feasible to speculate that reducing the amount of Cr in alloys will mitigate the effect of hydrogen. Higher dislocation density plays a more profound role in the hydrogen hardening effect compared to the solute drag stress, meaning the increase of initial dislocation density due to the decrease of the free energy of homogeneous dislocation nucleation is assumed to play a more critical role in HE.

Data availability

Data will be made available on request.

Declaration of Competing Interest

The authors declare that they have no known competing financial interests or personal relationships that could have appeared to influence the work reported in this paper.

Acknowledgements

The project was funded by the German research foundation (Deutsche Forschungsgemeinschaft, DFG) in project number 318876084 "hydrogen-microstructure interactions in ferritic alloys at small scale". Gerhard Dehm and María Jazmin Duarte acknowledge financial support by the ERC grant GB correlate (787446). Jing Rao acknowledges financial support by the KSB foundation for the final stage of her studies.

Appendix A. Supplementary data

Supplementary data to this article can be found online at https://doi.org/10.1016/j.matdes.2023.112143.

References

[1] B. Sun, D. Wang, X. Lu, D. Wan, D. Ponge, X. Zhang, Current Challenges and Opportunities Toward Understanding Hydrogen Embrittlement Mechanisms in Advanced High-Strength Steels, A Review, Acta Metall. Sin. (2021) 1–14.
[2] H. Zhao, P. Chakraborty, D. Ponge, T. Hickel, B. Sun, C.-H. Wu, B. Gault, D. Raabe, Hydrogen trapping and embrittlement in high-strength Al-alloys, Nature 602 (7897) (2022) 437–441.
[3] A. Drexler, F. Konert, O. Sobol, M. Rhode, J. Domitner, C. Sommitsch, T. Böllinghaus, Enhanced gaseous hydrogen solubility in ferritic and martensitic steels at low temperatures, Int. J. Hydrogen Energy 47 (93) (2022) 39639–39653.
[4] E.R. Hans Jürgen Grabke, Absorption and diffusion of hydrogen in steels, Mater. Tehnol. 34(6) (2000) 331.
[5] A. Hadadzadeh, A. Shahriari, B.S. Amirkhiz, J. Li, M. Mohammadi, Additive manufacturing of an Fe–Cr–Ni–Al maraging stainless steel: microstructure evolution, heat treatment, and strengthening mechanisms, Mater. Sci. Eng., A 787 (2020) 139470.
[6] A. Shirley, C. Hall, Trapping of hydrogen by substitutional and interstitial impurities in α-iron, Scr. metall. 17 (8) (1983) 1003–1008.
[7] H.K.D.H. Bhadeshia, Prevention of hydrogen embrittlement in steels, ISIJ Int. 56 (1) (2016) 24–36.
[8] R. Andreas, S. Oded, H. Hannu, T. Böllinghaus, In-situ ToF-SIMS analyses of deuterium re-distribution in austenitic steel AISI 304L under mechanical load, Sci. Rep. 10 (1) (2020).
[9] J.-M. Park, Y. Zhao, T. Voisin, D.-H. Lee, S.-I. Komazaki, Y. Ko, D.-I. Kim, J.-Y. Suh, H.N. Han, Y.M. Wang, U. Ramamurty, J.-i. Jang, Hydrogen uptake and its influence in selective laser melted austenitic stainless steel: A nanoindentation study, Scripta Mater. 194 (2021) 113718.
[10] B. Sun, W. Krieger, M. Rohwerder, D. Ponge, D. Raabe, Dependence of hydrogen embrittlement mechanisms on microstructure-driven hydrogen distribution in medium Mn steels, Acta Mater. 183 (2020) 313–328.
[11] D. An, Y. Zhou, Y. Xiao, X. Liu, X. Li, J. Chen, Observation of the Hydrogen-Dislocation Interactions in a High-Manganese Steel after Hydrogen Adsorption and Desorption, Acta Metall. Sin. 36 (7) (2023) 1105–1112.
[12] A. Massone, A. Manhard, W. Jacob, A. Drexler, W. Ecker, A. Hohenwarter, S. Wurster, D. Kiener, An SEM compatible plasma cell for in situ studies of hydrogen-material interaction, Rev. Sci. Instrum. 91 (4) (2020) 043705.
[13] L. Huang, D. Chen, D. Xie, S. Li, Y. Zhang, T. Zhu, D. Raabe, E.n. Ma, J.u. Li, Z. Shan, Quantitative tests revealing hydrogen-enhanced dislocation motion in α-iron, Nat. Mater. 22 (6) (2023) 710–716.
[14] A. Barnoush, H. Vehoff, Electrochemical nanoindentation: A new approach to probe hydrogen/deformation interaction, Scripta Mater. 55 (2) (2006) 195–198.
[15] A. Barnoush, H. Vehoff, In situ electrochemical nanoindentation: A technique for local examination of hydrogen embrittlement, Corros. Sci. 50 (1) (2008) 259–267.
[16] A. Barnoush, H. Vehoff, Recent developments in the study of hydrogen embrittlement: Hydrogen effect on dislocation nucleation, Acta Mater. 58 (16) (2010) 5274–5285.
[17] R. Kirchheim, Solid solution softening and hardening by mobile solute atoms with special focus on hydrogen, Scripta Mater. 67 (9) (2012) 767–770.
[18] D. Wang, X. Lu, Y. Deng, X. Guo, A. Barnoush, Effect of hydrogen on nanomechanical properties in Fe-22Mn-0.6C TWIP steel revealed by in-situ electrochemical nanoindentation, Acta Mater. 166 (2019) 618–629.
[19] X. Lu, D. Wang, Effect of hydrogen on deformation behavior of Alloy 725 revealed by in-situ bi-crystalline micropillar compression test, J. Mater. Sci. Technol. 67 (2021) 243–253.
[20] D. Wang, X. Lu, M. Lin, D. Wan, Z. Li, J. He, R.J.J.o.M.S. Johnsen, Technology, Understanding the hydrogen effect on pop-in behavior of an equiatomic high-entropy alloy during in-situ nanoindentation, 98 (2022) 118-122.

[21] A.S. Ebner, S. Brinckmann, E. Plesiutschnig, H. Clemens, R. Pippan, V. Maier-Kiener, A Modified Electrochemical Nanoindentation Setup for Probing Hydrogen-Material Interaction Demonstrated on a Nickel-Based Alloy, Jom 72 (5) (2020) 2020–2029.
[22] M. Duarte, X. Fang, J. Rao, W. Krieger, S. Brinckmann, G. Dehm, In situ nanoindentation during electrochemical hydrogen charging: a comparison between front-side and a novel back-side charging approach, J. Mater. Sci. 1–13 (2021).
[23] A. Ahmadian, D. Scheiber, X. Zhou, B. Gault, C. Liebscher, L. Romaner, G. Dehm, Aluminum depletion induced by co-segregation of carbon and boron in a bcc-iron grain boundary, Nat. Commun. 12 (1) (2021) 1–11.
[24] Y.-U. Heo, Comparative study on the specimen thickness measurement using EELS and CBED methods, Appl. Microsc. 50 (1) (2020) 8.
[25] J. Schindelin, I. Arganda-Carreras, E. Frise, V. Kaynig, M. Longair, T. Pietzsch, S. Preibisch, C. Rueden, S. Saalfeld, B. Schmid, Fiji: an open-source platform for biological-image analysis, Nat. Methods 9 (7) (2012) 676–682.
[26] D. Geng, H. Yu, Y. Okuno, S. Kondo, R. Kasada, Practical method to determine the effective zero-point of indentation depth for continuous stiffness measurement nanoindentation test with Berkovich tip, Sci. Rep. 12 (1) (2022) 1–7.
[27] W.C. Oliver, G.M. Pharr, Measurement of hardness and elastic modulus by instrumented indentation: Advances in understanding and refinements to methodology, J. Mater. Res. 19 (1) (2004) 3–20.
[28] S. Manisha, S. Vinoth, M.S. Shunmugaraj, M.M. Kumar, Y.P. Yadav, Double skin rubberized steel fiber mixed composite column, Mater. Today 68 (2022) 2175–2181.
[29] B.D. Beake, S.R. Goodes, J.F. Smith, Nanoscale materials testing under industrially relevant conditions: high-temperature nanoindentation testing, Int. J. Mater. Res. 94 (7) (2022) 798–801.
[30] A. Atrens, Q. Liu, C. Tapia-Bastidas, E. Gray, B. Irwanto, J. Venezuela, Q. Liu, Influence of Hydrogen on Steel Components for Clean Energy, Corros. mater. degrad. 1 (1) (2018) 3–26.
[31] Q. Liu, A. Atrens, A critical review of the influence of hydrogen on the mechanical properties of medium-strength steels, Corros. Rev. 31 (3–6) (2013) 85–103.
[32] Y. Yao, X. Pang, K. Gao, Investigation on hydrogen induced cracking behaviors of Ni-base alloy, Int. J. Hydrogen Energy 36 (9) (2011) 5729–5738.
[33] E. Dafft, K. Bohnenkamp, H. Engell, Investigations of the hydrogen evolution kinetics and hydrogen absorption by iron electrodes during cathodic polarization, Corros. Sci. 19 (9) (1979) 591–612.
[34] L. Marchetti, E. Herms, P. Laghoutaris, J. Chene, Hydrogen embrittlement susceptibility of tempered 9% Cr–1% Mo steel, Int. J. Hydrogen Energy 36 (24) (2011) 15880–15887.
[35] S. Asano, Y. Nishino, R. Otsuka, Lattice Hardening and Anomalous Softening of Iron and Steel Caused by Electrolytic Hydrogen Charging, J. Jpn. Inst. Met. 43 (3) (1979) 241–248.
[36] S. Wang, N. Hashimoto, S. Ohnuki, Effects of hydrogen on activation volume and density of mobile dislocations in iron-based alloy, Mater. Sci. Eng., A 562 (2013) 101–108.
[37] K.-E. Thelning, Steel and its heat treatment, Butterworth-heinemann2013.
[38] M. Maalekian, The effects of alloying elements on steels (I), (2007).
[39] C. Heintze, F. Bergner, M. Hernández-Mayoral, Ion-irradiation-induced damage in Fe–Cr alloys characterized by nanoindentation, J. Nucl. Mater. 417 (1–3) (2011) 980–983.
[40] D. Caillard, A TEM in situ study of alloying effects in iron. II—Solid solution hardening caused by high concentrations of Si and Cr, Acta Mater. 61 (8) (2013) 2808–2827.
[41] M. Matijasevic, A. Almazouzi, Effect of Cr on the mechanical properties and microstructure of Fe–Cr model alloys after n-irradiation, J. Nucl. Mater. 377 (1) (2008) 147–154.
[42] K. Durst, B. Backes, O. Franke, M. Göken, Indentation size effect in metallic materials: Modeling strength from pop-in to macroscopic hardness using geometrically necessary dislocations, Acta Mater. 54 (9) (2006) 2547–2555.
[43] K.L. Johnson, Contact Mechanics, ninth printing, Cambridge University Press, 2003.
[44] M.M. Biener, J. Biener, A.M. Hodge, A.V. Hamza, Dislocation nucleation in bcc Ta single crystals studied by nanoindentation, Phys. Rev. B 76 (16) (2007) 165422.
[45] W.D. Nix, H. Gao, Indentation size effects in crystalline materials: a law for strain gradient plasticity, J. Mech. Phys. Solids 46 (3) (1998) 411–425.
[46] W.S. Choi, B.C. De Cooman, S. Sandlöbes, D. Raabe, Size and orientation effects in partial dislocation-mediated deformation of twinning-induced plasticity steel micro-pillars, Acta Mater. 98 (2015) 391–404.
[47] J. Rosenberg, H. Piehler, Calculation of the Taylor factor and lattice rotations for bcc metals deforming by pencil glide, Metall. Trans. B 2 (1) (1971) 257–259.
[48] G.I. Taylor, The mechanism of plastic deformation of crystals. Part I.—Theoretical, Proc. R. Soc. Lond. A 145(855) (1934) 362-387.
[49] X. Qiu, Y. Huang, W. Nix, K. Hwang, H. Gao, Effect of intrinsic lattice resistance in strain gradient plasticity, Acta Mater. 49 (19) (2001) 3949–3958.
[50] G. Ghosh, G. Olson, The isotropic shear modulus of multicomponent Fe-base solid solutions, Acta Mater. 50 (10) (2002) 2655–2675.
[51] H. Hagi, Y. Hayashi, Effects of interstitial impurities on dislocation trapping of hydrogen in iron, Trans. Jpn. Inst. Met. 28 (5) (1987) 375–382.
[52] D.P. Abraham, C.J. Altstetter, The effect of hydrogen on the yield and flow stress of an austenitic stainless steel, Metall. Mater. Trans. A 26 (11) (1995) 2849–2858.
[53] R. Oriani, P. Josephic, Effects of hydrogen on the plastic properties of medium-Carbon steels, Metall. Trans. A 11 (11) (1980) 1809–1820.
[54] P.M. Anderson, J.P. Hirth, J. Lothe, Theory of dislocations, Cambridge University Press, 2017.
[55] J. Song, W.A. Curtin, Mechanisms of hydrogen-enhanced localized plasticity: An atomistic study using α-Fe as a model system, Acta Mater. 68 (2014) 61–69.
[56] P. El Ters, M.A. Shehadeh, Modeling the temperature and high strain rate sensitivity in BCC iron: Atomistically informed multiscale dislocation dynamics simulations, Int. J. Plast. 112 (2019) 257–277.
[57] A. Barnoush, M. Asgari, R. Johnsen, Resolving the hydrogen effect on dislocation nucleation and mobility by electrochemical nanoindentation, Scripta Mater. 66 (6) (2012) 414–417.
[58] G. Leyson, B. Grabowski, J. Neugebauer, Multiscale description of dislocation induced nano-hydrides, Acta Mater. 89 (2015) 50–59.
[59] L. Pauling, The Nature of the Chemical Bond, Cornell university press Ithaca, NY1960.
[60] V.P. Ramunni, C. Hurtado-Noreña, P. Bruzzoni, Ab-initio approach to study hydrogen diffusion in 9Cr steels, Phys. B Condens. Matter 407 (16) (2012) 3301–3304.
[61] I. Maroef, D. Olson, M. Eberhart, G. Edwards, Hydrogen trapping in ferritic steel weld metal, Int. Mater. Rev. 47 (4) (2002) 191–223.
[62] M. Nagumo (Ed.), Fundamentals of Hydrogen Embrittlement, Springer Singapore, Singapore, 2016.
[63] D. Jiang, E.A. Carter, Diffusion of interstitial hydrogen into and through bcc Fe from first principles, Phys. Rev. B 70 (6) (2004) 064102.
[64] J. Crank, The mathematics of diffusion, Oxford university press1979.
[65] N. Barakat, Hydrogen permeation through low alloy steels, Heriot-Watt University, 2009.
[66] S.K. Lawrence, B.P. Somerday, M.D. Ingraham, D.F. Bahr, Probing the effect of hydrogen on elastic properties and plastic deformation in nickel using nanoindentation and ultrasonic methods, Jom 70 (7) (2018) 1068–1073.
[67] N. Paton, O. Buck, J. Williams, Effect of hydrogen on the strength modulus and lattice parameter of a Ti–Mo alloy, Scr. metall. 9 (6) (1975) 687–691.
[68] E. Fisher, D. Westlake, S. Ockers, Effects of hydrogen and oxygen on the elastic moduli of vanadium, niobium, and tantalum single crystals, phys, stat. sol. (a) 28 (2) (1975) 591–602.
[69] U. Hadam, T. Zakroczymski, Absorption of hydrogen in tensile strained iron and high-carbon steel studied by electrochemical permeation and desorption techniques, Int. J. Hydrogen Energy 34 (5) (2009) 2449–2459.
[70] T.-Y. Zhang, F.-X. Jiang, W.-Y. Chu, C.-M. Hsiao, Effect of hydrogen on the Young's modulus of iron, Metall. Trans. A 16 (9) (1985) 1655–1662.